

# Unpaired Optical Coherence Tomography Angiography Image Super-Resolution via Frequency-Aware Inverse-Consistency GAN

Weiwen Zhang, Dawei Yang, Haoxuan Che, *Student Member, IEEE* An Ran Ran, Carol Y. Cheung, and Hao Chen, *Senior Member, IEEE*

arXiv:2309.17269v1 [eess.IV] 29 Sep 2023

**Abstract**—For optical coherence tomography angiography (OCTA) images, a limited scanning rate leads to a trade-off between field-of-view (FOV) and imaging resolution. Although larger FOV images may reveal more parafoveal vascular lesions, their application is greatly hampered due to lower resolution. To increase the resolution, previous works only achieved satisfactory performance by using paired data for training, but real-world applications are limited by the challenge of collecting large-scale paired images. Thus, an unpaired approach is highly demanded. Generative Adversarial Network (GAN) has been commonly used in the unpaired setting, but it may struggle to accurately preserve fine-grained capillary details, which are critical biomarkers for OCTA. In this paper, our approach aspires to preserve these details by leveraging the frequency information, which represents details as high-frequencies ( $hf$ ) and coarse-grained backgrounds as low-frequencies ( $lf$ ). In general, we propose a GAN-based unpaired super-resolution method for OCTA images and exceptionally emphasize  $hf$  fine capillaries through a dual-path generator. To facilitate a precise spectrum of the reconstructed image, we also propose a frequency-aware adversarial loss for the discriminator and introduce a frequency-aware focal consistency loss for end-to-end optimization. Experiments show that our method outperforms other state-of-the-art unpaired methods both quantitatively and visually.

**Index Terms**—OCT-Angiography, Unpaired Super-Resolution, GAN, Frequency Analysis

## I. INTRODUCTION

Optical coherence tomography angiography (OCTA) is an imaging modality based on the optical coherence tomography

This work was supported by funding from HKUST 30 for 30 Research Initiative Scheme, Hong Kong University of Science and Technology, and Shenzhen Science and Technology Innovation Committee (Project No. SGDX20210823103201011), and Direct Grants from The Chinese University of Hong Kong (Project Code: 4054419 & 4054487). (*Corresponding author: Hao Chen.*)

Weiwen Zhang and Haoxuan Che are with the Department of Computer Science and Engineering, The Hong Kong University of Science and Technology, Hong Kong, China (e-mail: wzhangbu@cse.ust.hk; hche@cse.ust.hk).

Dawei Yang, An Ran Ran, and Carol Y. Cheung are with the Department of Ophthalmology and Visual Sciences, The Chinese University of Hong Kong, Hong Kong, China (e-mail: gabrielyang@link.cuhk.edu.hk; emma\_anran@link.cuhk.edu.hk; carolcheung@cuhk.edu.hk).

Hao Chen is with the Department of Computer Science and Engineering, The Hong Kong University of Science and Technology, Hong Kong, China, and also with the Department of Chemical and Biological Engineering, The Hong Kong University of Science and Technology, Hong Kong, China (e-mail: jhc@cse.ust.hk).

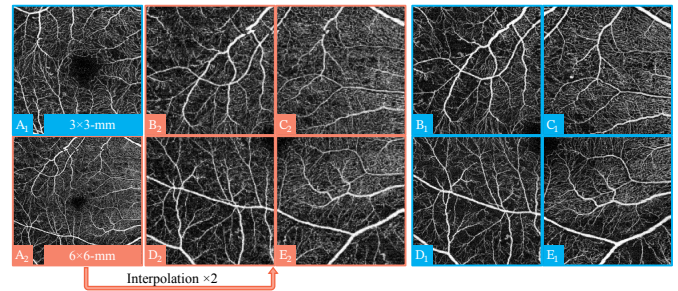


Fig. 1. Illustration for our OCTA images dataset, which is retrospectively collected from the Chinese University of Hong Kong Sight-Threatening Diabetic Retinopathy (CUHK-STDR) study. Orange boxes indicate the 6mm×6mm with subscript 1, while blue boxes indicate the 3mm×3mm with subscript 2. The same letter indicates the same regions in low- and high-resolution images. A: Fovea-center. B~E: parafoveal patches.

(OCT) platform, which generates depth-resolved images of the retina and choroidal microvasculature [1]. OCTA can support the evaluation of multiple retinal diseases, including diabetic retinopathy and age-related macular degeneration [2]–[7]. However, due to the limited scanning rate of commercial OCT instruments [8], [9], images with a smaller field-of-view (FOV) have higher axial scan density and thus higher resolution [10]. As a result, among most common FOV, 3mm×3mm (Fig. 1.  $A_1 \sim E_1$ ) is more widely employed in clinical settings to visualize finer capillaries, as compared to the 6mm×6mm [7], [11]. Nevertheless, larger FOV (Fig. 1.  $A_2$ ) is supposed to reveal more parafoveal vascular lesions [12]. Therefore, improving the resolution of 6mm×6mm images (Fig. 1.  $A_2$ ), on par with 3mm×3mm images, will further empower ophthalmologists to evaluate capillary losses and develop more personalized treatments [13]–[15]. In computer vision, this task refers to super-resolution which upscales images (Fig. 1.  $A_2$  to  $B_2 \sim E_2$ ) and improves the quality through restoration.

For OCTA image super-resolution, only a few works have been proposed and most adopt the paired setting for training to achieve the desired qualitative performance [9], [16], [17]. One approach involves collecting and creating paired high-resolution ( $HR$ ) and low-resolution ( $LR$ ) images from the same eye of the same patient [9], [16]. However, collecting large-scale real-paired images requires sophisticated image registration, which is laborious and challenging and may

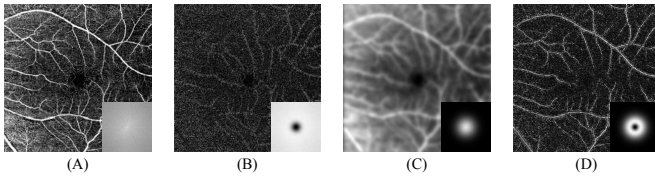


Fig. 2. Illustration for  $6\text{mm} \times 6\text{mm}$  OCTA images and frequency components. Lower-right corners are bandwidth spectral filters. A:  $6\text{mm} \times 6\text{mm}$  OCTA image and its spectrum. B:  $lf$  and its low-pass filter. C:  $hf$  and its high-pass filter. D: Middle-frequencies and its middle-pass filter.

hinder the medical application [18]. Another approach creates pseudo image pairs using bicubic interpolation to synthesize  $LR$  from  $HR$  for training [17]. However, interpolation is an oversimplified presumption since it may not accurately represent real-world degradation. Alternatively, the unpaired setting could mitigate these issues, but there is still a lack of sufficient studies. Therefore, we propose an unpaired approach by formulating a degradation model and jointly optimizing the models [19]. Also regarding the consensual merits of Generative Adversarial Networks (GANs), the models are accordingly formulated and optimized via consistency loss [20]–[24].

Moreover, higher resolution of the capillary network will allow more accurate assessments of eye diseases related to microvasculature [25], [26]. Thus the algorithm should exceptionally emphasize the fine-grained vessels. In the frequency domain, these vessels correspond to high-frequency ( $hf$ ) information (Fig. 2. B), whereas the general illuminance and backgrounds correspond to low frequencies ( $lf$ ) (Fig. 2. C). However, convolutional neural networks (CNNs) inherently exhibit a bias towards  $lf$  [27]. This bias can also be observed in the spectral distribution (Fig. 3), which illustrates a discernibly increasing discrepancy between reconstructed images and  $HR$  ground truths as the bandwidth increases. Though super-resolution aspires to enhance  $hf$  details, such bias may result in inaccurate or deficient details [28]–[30]. Consequently, for OCTA images, capillary structures in microvasculature might be altered. To alleviate these issues, our approach directly leverages frequency information and imposes exceptional emphasis on  $hf$ , aiming at accurate and sufficient fine-grained details. Specifically in our restoration and degradation GAN, to preserve salient  $hf$  details in generators, we separate frequency components in a dual-path structure for feature extraction and then fuse features for reconstruction. To also facilitate discriminators being sensitive to  $hf$ , we introduce the frequency-aware adversarial loss (FAL) to consider both frequency and spatial components. To consistently preserve the frequency distribution, we propose a Frequency-aware Focal Consistency Loss (FFCL).

In general, by leveraging frequency information and imposing exceptional emphasis on  $hf$ , this paper introduces a Frequency-aware Unpaired Super-Resolution for OCTA images (FAUSRA). To surmount  $lf$ -bias of neural networks, we propose a dual-path architecture in generators to separately refine  $hf$  capillary details. To also facilitate discriminators being aware of frequencies, we propose FAL by exploiting wavelet space. To preserve accurate spectral distribution, we propose the FFCL to penalize spectral errors. Then, our approach

exploits both frequency and spatial domains to effectively produce high-resolution images in the unpaired setting.

This paper contributes in following perspectives:

- To resolve the unpaired OCTA super-resolution, we propose a GAN-based approach containing restoration and degradation models, and jointly optimize it using consistency losses in an end-to-end manner.
- To mitigate  $lf$ -bias and enhance fine-grained details, we exceptionally emphasize  $hf$  components in a dual-path structure in generators. We also propose FAL for adversarial training, and the FFCL for spectral consistency.
- To quantitatively evaluate the performance, we purposely collect fovea-central and parafoveal paired  $HR$  and  $LR$  images from CUHK-STDR study for different paired metrics, and verify the superiority of our method.

## II. RELATED WORKS

**Super-Resolution** has been a prominent task in low-level computer vision, aimed at increasing the resolution and restoring imaging quality, including OCTA images [9]. In recent years, with the advancements in deep learning, learning-based techniques have demonstrated remarkable performance, particularly through supervised learning using paired datasets [31]. However, for most imaging modalities in the real world, the challenge of collecting large-scale paired datasets remained a fundamental issue [32]. To overcome this challenge, a common approach was to generate training data by downsampling  $HR$  images to synthetic  $LR$  counterparts using interpolation [31]. Subsequently, algorithms aimed to recover the super-resolution mapping by restoring  $LR$ . However, interpolation-based downsampling oversimplified the degradation process, leading to models that may not generalize well to real-world super-resolution. To relieve the issues under the paired setting, GAN has been introduced [33]. Adversarial loss guided the model to produce more visually pleasing results [20], but these methods still rely on paired data for training.

**Unpaired Super-Resolution** methods alternatively employed various models to formulate the degradation process. These methods could be categorized into two main approaches: **two-stage** and **one-stage** methods.

**Two-Stage** methods primarily formulated the degradation process, followed by a separate optimization of the restoration model. [34] proposed a kernel estimation approach to mimic real-world degradation. [19] introduced a High-to-Low GAN, which generates the  $LR$  from  $HR$ . To ensure stable optimization of the degradation, [35] proposed to synthesize  $LR$  and utilized unsupervised learning to bridge the gap between real and synthesized images. However, for two-stage approaches, the restoration might be highly affected by the performance of degradation, causing suboptimal restoration results [36].

**One-Stage** approaches commonly employed GAN and consistency loss to jointly optimize the models end-to-end [24]. For instance, a bi-cycle network was proposed to jointly generate real-world  $LR$  and optimize the super-resolution model [21]. However, GAN has suffered from instability in the training phase and thus is prone to introduce unexpected noises [37], [38]. To this end, several solutions were proposed.

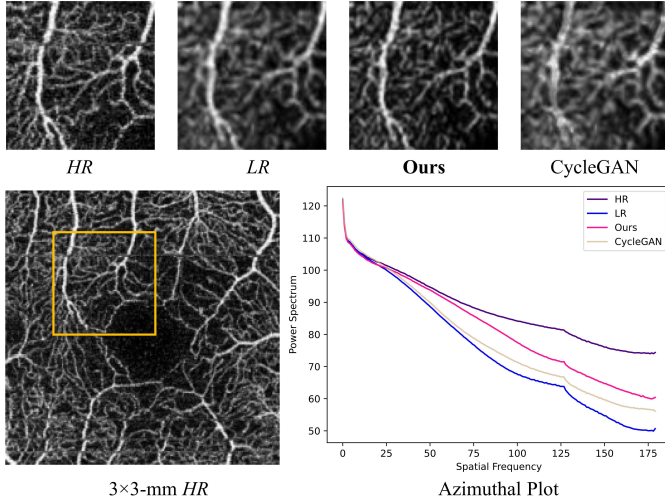


Fig. 3. Azimuthal integral on spectrum as specified in Eq. (2). It indicates that *HR* contains stronger power in middle- and high-bands of the spectrum than *LR*. While the middle frequencies of different methods are similar, our approach better fits the *lf* information and enhances *hf* information compared to the real *HR*.

Some modified the architecture of the pipeline. [22] proposed a cycle-in-cycle structure using nested GANs and consistency losses. [23] proposed a pseudo-supervision using corrected-clean and pseudo-clean *LR* as intermediates between *LR* and *HR* images. Another attempt was to introduce frequency information. By exploiting both spatial and wavelet domains, [32] resolved unpaired super-resolution via domain adaptation to tackle the gap between real and synthetic images.

**OCTA Super-Resolution** algorithms specifically aimed to upscale  $6\text{mm} \times 6\text{mm}$  images and improve their quality on a par with  $3\text{mm} \times 3\text{mm}$  images. However, the preparation of training OCTA images posed a laborious challenge [18]. Existing methods addressed this challenge by either synthesizing *LR* or collecting paired images. For example, [17] proposed a method that degrades *HR* images through interpolation down-sampling. Although this approach intended to mitigate domain gaps between real- and generated images using GAN, the restoration modeling overlooked complex real-world degradation, which could be influenced by different FOV, limited scanning rates, etc. Alternative methods veritably collected paired *HR* and *LR* images from the same eye of the same patient and employed a supervised approach to enhance the *LR* images [9], [16]. However, these approaches suffered from two inherent limitations when applied to OCTA images. Firstly, to prepare pixel-wise paired images for training and evaluation, registration should be used to mitigate structural changes from image capturing. Such preprocessing inevitably altered the original structure within the OCTA image, resulting in unconvincing supervision. Secondly, due to different FOV, each  $3\text{mm} \times 3\text{mm}$  image could only provide incomplete supervision with only a sub-region of *HR* information for each  $6\text{mm} \times 6\text{mm}$  image. The above limitations motivated our unpaired OCTA super-resolution, which could release the reliance on paired data and implicitly formulate the restoration and degradation using GAN.

**Frequency Analysis Studies** showed that deep neural net-

works tend to fit *lf* more precisely than *hf* [27]. Especially for GANs that are commonly utilized in unpaired super-resolution, models also suffered from the bias and resulted in missing *hf* details or unexpected artifacts [37], [38]. The spectral distribution can also demonstrate this bias, where *hf* were not reconstructed as sufficiently as *lf* (see Fig. 3). To produce high-fidelity *HR* images, *hf* capillary details [39] should have been meticulously preserved. To address this inherent gap, frequency information has been included in deep learning frameworks by separating frequency components [40]. [41] leveraged frequency components in unpaired super-resolution algorithm. In addition to incorporating frequency in the frameworks, several frequency-aware losses have been introduced to yield more realistic results. [28] proposed exploiting the wavelet domain to mitigate the domain gap between real and synthetic images. [29] introduced Frequency Consistent Adaptation to ensure frequency domain consistency. The focal frequency loss [42] adaptively focused on frequency components using amplitude and phase information. [39] suggested a Fourier frequency loss to separately preserve high and low-frequency amplitudes. However, studies that use frequency and spatial information for unpaired OCTA super-resolution have not been sufficiently conducted yet.

Therefore, under the unpaired super-resolution setting, this paper proposes leveraging spatial and different frequency components in the restoration and degradation frameworks to benefit unpaired super-resolution. To reconstruct precise frequency information, we introduce **FAL** for discriminators and the **FFCL** for our end-to-end framework.

### III. METHODOLOGY

To resolve unpaired super-resolution for OCTA images, we propose GAN-based restoration and inverse degradation models, which are optimized in an end-to-end manner through consistency loss [24], as depicted in Fig. 4. To mitigate the frequency bias and thus precisely enhance *hf* capillary details, we leverage different frequency components via a dual-path structure within the framework. In the GAN paradigm, we also exploit the frequency domain through **FAL** for the discriminators, and propose an **FFCL** to guarantee accurate spectrum as an objective for end-to-end learning.

#### A. Preliminaries

We define  $3\text{mm} \times 3\text{mm}$  OCTA images as the *HR* and  $6\text{mm} \times 6\text{mm}$  images as the *LR*. We denote the restoration process as the mapping from *LR* to *HR*, represented by  $G_{Res} : LR \rightarrow HR^\uparrow$ , and the degradation process as the inverse mapping from *HR* to *LR*, represented by  $G_{Deg} : HR \rightarrow LR^\downarrow$ . Here,  $HR^\uparrow$  and  $LR^\downarrow$  refer to the generated *HR* and *LR* images.

Without loss of generality, we denote an image  $x \in \mathbb{R}^{M \times N}$  which can be either *HR* or *LR*. Then its frequency representation is denoted as  $\mathcal{X}$ . The Fast Fourier Transformation (FFT) transforms  $x$  to  $\mathcal{X}$  as:

$$\begin{aligned} \mathcal{X}(u, v) &= \sum_{m=0}^{M-1} \sum_{n=0}^{N-1} x(m, n) e^{-i2\pi(\frac{um}{M} + \frac{vn}{N})} \\ &= R(u, v) + iI(u, v) \end{aligned} \quad (1)$$

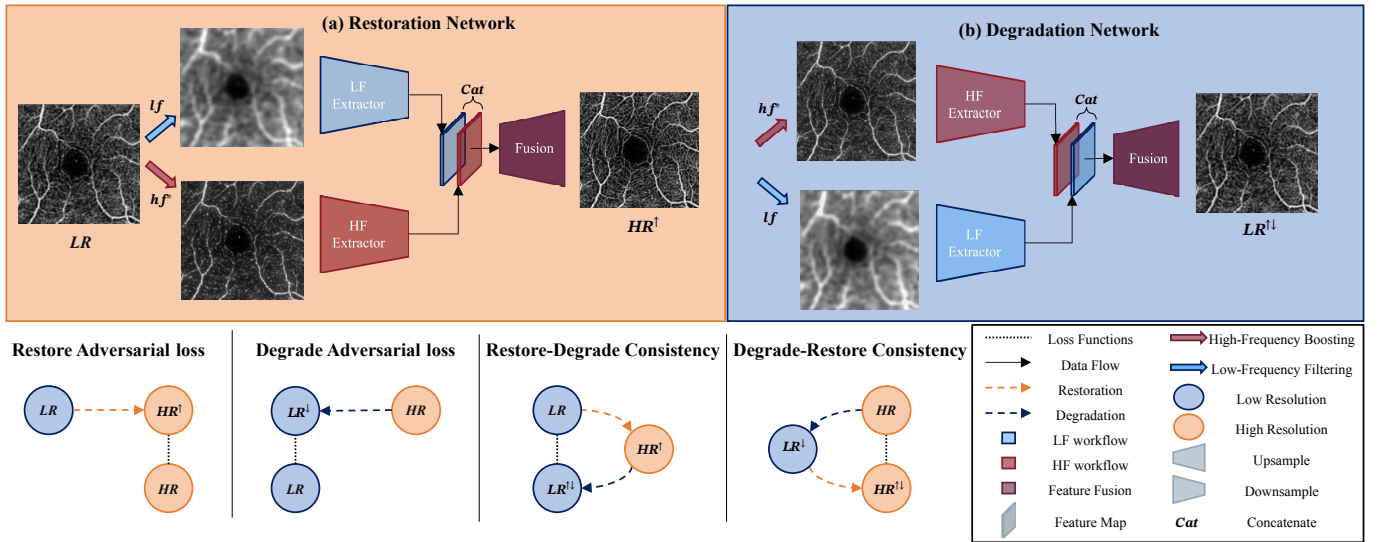


Fig. 4. An overview of our methods. An input low-resolution image  $LR$  is restored and then degraded through restoration-degradation consistency. The input  $LR$  is first decomposed into  $lf$  and  $hf^*$  (through  $HFB$ ) and then fused for reconstruction. Eventually, restoration is taken as OCTA high-resolution model in the inference phase. The inverse degradation-restoration process is represented in simplified conceptual graphs.

where  $M$  and  $N$  are image height and width, while  $(m, n)$  and  $(u, v)$  are Cartesian coordinates of the image in the spatial and frequency domain. Since FFT results are complex numbers,  $\mathcal{X}$  can be further separated into real ( $R$ ) and imaginary parts ( $I$ ) with respect to Euler's formula  $e^{i\theta} = \cos\theta + i\sin\theta$ .

Based on FFT, to visualize the spectral power, the azimuthal integral over the spectrum is defined as [43]:

$$A(\omega_k) = \int_0^{2\pi} \|\mathcal{X}(\omega_k \cdot \cos(\phi), \omega_k \cdot \sin(\phi))\|^2 d\phi \quad (2)$$

where  $(\phi, \omega_k)$  is the azimuth and  $k$ -bandwidth in polar coordinate of the image, and  $k = 0, 1, \dots, M/2 - 1$ .

To leverage frequency information by high- and low-pass filters, we first define the Gaussian kernel as:

$$G(u, v) = \frac{1}{2\pi\sigma^2} e^{-(u^2+v^2)/(2\sigma^2)} \quad (3)$$

where  $\sigma$  is the variance of Gaussian kernel, and  $(u, v)$  is Cartesian coordinate. Thus the  $lf$  is extracted by Gaussian blurring using convolution operation,  $lf = G * x$ . The  $hf$  is obtained by subtracting the  $lf$  information from the original image,  $hf = x - lf$ . Gaussian blurry in the spatial domain can be represented as low-pass filtering in the frequency domain according to the convolution theorem (see Fig. 2).

## B. Frequency-aware Restoration and Degradation

In our unpaired setting, we propose a one-stage end-to-end super-resolution pipeline by formulating the restoration model  $G_{Res}$  and a degradation model  $G_{Deg}$ . Models are optimized according to adversarial loss and consistency loss [20], [24].

Super-resolution aims to effectively and accurately refine fine-grained details. In the frequency domain, these details are widely recognized as  $hf$ , while contours are referred to as  $lf$  [44]. But limited by the inherent bias of neural networks,  $hf$  may not be sufficiently boosted [27]. Therefore, our work proposes a frequency-aware architecture that leverages both spatial and frequency information, as shown in Fig. 4.

Specifically, to emphasize  $hf$  and alleviate the bias to  $lf$ , we intentionally separate frequency components using Gaussian filtering, as shown in Eq. (3), and extract corresponding features through a dual-path structure (see Fig. 4(a) and (b)). Then, the images are reconstructed by fusing these features. Such that the restoration model,  $G_{Res}$ , enhances  $hf$  details while preserving  $lf$  backgrounds. For the degradation model,  $G_{Deg}$ ,  $hf$  details are filtered out while  $lf$  components are retained. Additionally, to provide  $hf$  for generators, we define an operation dubbed as the high-frequency boosting ( $HFB$ ), in the following form:

$$hf^* = x + \alpha * hf \quad (4)$$

where  $hf^*$  represents the boosted  $hf$ , and  $\alpha$  is the factor determining the extent of enhancement. Since providing pure  $hf$  to the network may break vessel structures and cause incoherence, we utilize the  $HFB$  to obtain  $hf^*$ , shown in Eq. (4). Then  $lf$  and  $hf^*$  are provided as frequency components to the dual-path generators for feature extraction. Subsequently, the features are fused for the reconstruction.

To optimize the  $G_{Res}$  using the unpaired dataset, we incorporate consistency loss to preserve the vessel structures, namely inverse consistency since restoration and degradation represent inverse mappings between  $LR$  and  $HR$ . We formulate the degradation-restoration inverse-consistency,  $G_{Deg} \cdot G_{Res} : LR \rightarrow HR^{\uparrow} \rightarrow LR^{\downarrow}$ , using the  $L_1$  norm loss as:

$$\mathcal{L}_{inv}^{Res} (G_{Res}, G_{Deg}, LR) = \mathbb{E} [\|LR^{\downarrow} - LR\|_1] \quad (5)$$

The restoration-degradation inverse-consistency,  $G_{Res} \cdot G_{Deg} : HR \rightarrow LR^{\downarrow} \rightarrow HR^{\uparrow}$ , is also deployed to facilitate more precise training as:

$$\mathcal{L}_{inv}^{Deg} (G_{Deg}, G_{Res}, HR) = \mathbb{E} [\|HR^{\uparrow} - HR\|_1] \quad (6)$$

Furthermore, during the image translation using GAN, there is a lack of pixel-level regularization. Thus, common features shared by both  $LR$  and  $HR$  images will possibly be altered

when the generators are over-fitted, such as the morphology of vessels. Discriminators may not be capable of distinguishing these features and consequently overlook the alternations. To alleviate it, an identity loss is introduced to  $G_{Res}$  with the input being  $HR$ . This identity loss is formulated as follows:

$$\mathcal{L}_{idt}^{Res}(G_{Res}, HR) = \mathbb{E} [\|G_{Res}(HR) - HR\|_1] \quad (7)$$

To ensure the transitivity of the inverse workflow, we also introduce identity loss to  $G_{Deg}$  using  $LR$  as:

$$\mathcal{L}_{idt}^{Deg}(G_{Deg}, LR) = \mathbb{E} [\|G_{Deg}(LR) - LR\|_1] \quad (8)$$

Identity losses preserve vessel structures and suppress unexpected noises and artifacts in generating  $LR$  and  $HR$  images.

### C. Frequency-aware Adversarial Loss

Within Generative Adversarial Network (GAN), a powerful discriminator could induce a generator to produce high-quality results. As for the super-resolution, GAN aspires to produce  $HR$  images by accurately enhancing  $hf$  details while preserving  $lf$  contours. Therefore, we facilitate the discriminator in distinguishing frequency information and thus propose the frequency-aware adversarial loss (**FAL**).

Inspired by the superior performance of wavelets in discriminating frequency information [32], we decompose vertical and horizontal frequency components by applying either high-pass ( $H$ ) or low-pass ( $L$ ) Haar wavelets filters. Thus decomposed results include four possible combinations:  $LL$ ,  $LH$ ,  $HL$ , and  $HH$ , where  $L$  extracts  $lf$  and  $H$  extracts  $hf$ . Then we refer to all ( $LH$ ,  $HL$ ,  $HH$ ) as  $hf$ ,  $LL$  as  $lf$ , original image as spatial information, denoted as  $W_{hf}$ ,  $W_{lf}$ ,  $W_s$ , respectively (see Fig. 5). They are separately fed to three neural networks to capture frequency and spatial features, denoted as  $D_{hf}$ ,  $D_{lf}$ ,  $D_s$ . The final discrimination aggregates the outputs of three networks:

$$D(y) = D_{hf}(W_{hf}) + D_{lf}(W_{lf}) + D_s(W_s) \quad (9)$$

We employ two discriminators to distinguish between real and generated  $LR$  and  $HR$  images, denoted as  $D_{LR}$  and  $D_{HR}$ , respectively. By formulating  $D_{HR}$  using Eq. (9), the **FAL** for the  $G_{Res}$  is defined as:

$$\mathcal{L}_{\mathbf{FAL}}^{Res}(G_{Res}, D_{HR}, LR, HR) = \mathbb{E} \left[ \left\| D_{HR}(HR^\uparrow) - 1 \right\|^2 \right] + \mathbb{E} \left[ \left\| D_{HR}(HR) \right\|^2 \right] \quad (10)$$

where the labeling scheme considers real  $HR$  image as 1 and restored  $HR \uparrow$  image as 0. The mean square error is used, following the formulation of the least-square GAN [45]. Similarly, for the degradation counterpart, the **FAL** for  $G_{Deg}$  is defined as:

$$\mathcal{L}_{\mathbf{FAL}}^{Deg}(G_{Deg}, D_{LR}, LR, HR) = \mathbb{E} \left[ \left\| D_{LR}(LR^\downarrow) - 1 \right\|^2 \right] + \mathbb{E} \left[ \left\| D_{LR}(LR) \right\|^2 \right] \quad (11)$$

According to the essential paradigm of GAN [20], the Eq. (10) and (11) are minimized to optimize generators whereas being maximized to optimize the discriminators for distinguishing between real and generated data as sensitively as possible.

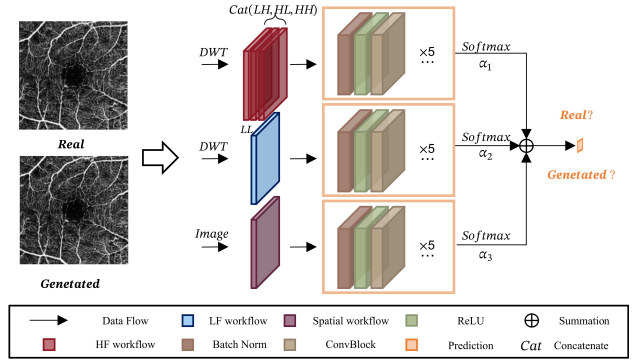


Fig. 5. Structure of the discriminator. Our method combines both frequency and spatial information in the discriminating phase. Results are aggregated to formulate the frequency-aware adversarial loss.

### D. Frequency-aware Consistency Focal Loss

To preserve the spectrum distribution in the reconstructed results of  $G_{Res}$  and  $G_{Deg}$ , we introduce a Frequency-aware Focal Consistency Loss (**FFCL**). Given the limitations of neural networks and GANs in accurately capturing  $hf$ , this term aims to enforce consistency in frequency information and place additional emphasis on  $hf$ .

Specifically, we first construct a spectrum weighting matrix to penalize the spectral consistency error as:

$$w(u, v) = |\mathcal{X}'(u, v) - \mathcal{X}(u, v)|^{\gamma_1} \quad (12)$$

where  $\mathcal{X}$  and  $\mathcal{X}'$  are the frequency representation of the original and reconstructed images  $x$  and  $x'$  via Eq. (1) [42].  $\gamma_1$  is the scaling factor. Then we formulate **FFCL** to penalize the error in the restoration and degradation consistency as:

$$\mathcal{L}_{\mathbf{FFCL}}(x, x') = \frac{1}{MN} \sum_{u=0}^{M-1} \sum_{v=0}^{N-1} w_{hf} \odot |\mathcal{X}'_{hf} - \mathcal{X}_{hf}|^2 + \gamma_2 w_{lf} \odot |\mathcal{X}'_{lf} - \mathcal{X}_{lf}|^2 \quad (13)$$

where  $u$  and  $v$  are coordinates of  $\mathcal{X}$  and  $\mathcal{X}'$ .  $w$  represents the spectrum weighting matrix using Eq. (12). The subscripts  $hf$  and  $lf$  indicate the  $hf$  and  $lf$  components, respectively.  $\gamma_2$  is a scaling factor. The symbol  $\odot$  denotes the Hadamard product, which applies the weighting matrix  $w$  to the mean square error between the spectra  $\mathcal{X}$  and  $\mathcal{X}'$ .

By aggregating all terms of our proposed loss functions, we form the final objective  $\mathcal{L}_{Total}$  as:

$$\min_G \max_D \mathcal{L}_{Total} = \left( \mathcal{L}_{\mathbf{FAL}}^{Deg} + \beta_1 \mathcal{L}_{\mathbf{FAL}}^{Res} \right) + \left( \mathcal{L}_{inv}^{Deg} + \beta_2 \mathcal{L}_{inv}^{Res} \right) + \left( \mathcal{L}_{idt}^{Deg} + \beta_3 \mathcal{L}_{idt}^{Res} \right) + \beta_4 \mathcal{L}_{\mathbf{FFCL}} \quad (14)$$

where  $G$  comprises both  $G_{Res}$  and  $G_{Deg}$ , while  $D$  consists of  $D_{HR}$  and  $D_{LR}$ . Then, the total loss  $\mathcal{L}_{Total}$  encompasses adversarial loss  $\mathcal{L}_{\mathbf{FAL}}$ , the consistency loss  $\mathcal{L}_{inv}$ , the identity loss  $\mathcal{L}_{idt}$ , and the frequency-aware focal consistency loss  $\mathcal{L}_{\mathbf{FFCL}}$ . The parameters  $\beta_1$ ,  $\beta_2$ ,  $\beta_3$ , and  $\beta_4$  in Eq. (14) are empirically set to 1, 10, 5, and 1 respectively. In the training phase, Eq. (14) is minimized to optimize the generators, while it is maximized to optimize the discriminator iteratively.

TABLE I

RESULTS OF DIFFERENT METHODS ON THE CUHK-STDR OF FOVEA-CENTRAL AND WHOLE AREA.  $\uparrow$  MEANS THE HIGHER THE BETTER.

Method	fovea-central area				whole area			
	PSNR $\uparrow$	SSIM $\uparrow$	NMI $\uparrow$	FSIM $\uparrow$	PSNR $\uparrow$	SSIM $\uparrow$	NMI $\uparrow$	FSIM $\uparrow$
CycleGAN-ResNet [24], [46]	16.827 $\pm$ 0.162	0.481 $\pm$ 0.003	1.054 $\pm$ 0.001	0.639 $\pm$ 0.003	17.183 $\pm$ 0.108	0.544 $\pm$ 0.002	1.059 $\pm$ 0.001	0.663 $\pm$ 0.001
CinCGAN [22]	16.991 $\pm$ 0.274	0.502 $\pm$ 0.025	1.052 $\pm$ 0.001	0.677 $\pm$ 0.014	17.177 $\pm$ 0.231	0.532 $\pm$ 0.013	1.056 $\pm$ 0.002	0.673 $\pm$ 0.005
Pseudo-Supervision [23]	17.193 $\pm$ 0.109	0.446 $\pm$ 0.008	1.054 $\pm$ 0.000	0.655 $\pm$ 0.002	17.611 $\pm$ 0.016	0.514 $\pm$ 0.009	1.062 $\pm$ 0.000	0.678 $\pm$ 0.002
DA-Unsupervised SR [28]	16.426 $\pm$ 0.073	0.426 $\pm$ 0.002	1.055 $\pm$ 0.000	0.616 $\pm$ 0.000	17.523 $\pm$ 0.197	0.513 $\pm$ 0.002	<b>1.064</b> $\pm$ <b>0.001</b>	0.651 $\pm$ 0.003
Frequency GAN [47]	17.435 $\pm$ 0.046	0.507 $\pm$ 0.003	1.057 $\pm$ 0.001	0.667 $\pm$ 0.004	17.547 $\pm$ 0.054	0.529 $\pm$ 0.004	1.061 $\pm$ 0.001	0.679 $\pm$ 0.004
<b>FAUSRA (Ours)</b>	<b>17.487</b> $\pm$ <b>0.034</b>	<b>0.512</b> $\pm$ <b>0.007</b>	<b>1.057</b> $\pm$ <b>0.001</b>	<b>0.679</b> $\pm$ <b>0.004</b>	<b>17.679</b> $\pm$ <b>0.072</b>	<b>0.555</b> $\pm$ <b>0.002</b>	<u>1.063</u> $\pm$ <u>0.000</u>	<b>0.689</b> $\pm$ <b>0.003</b>

TABLE II

RESULTS OF THE EXPERIMENTS ON FREQUENCY COMPONENTS ON THE CUHK-STDR OF FOVEA-CENTRAL AND WHOLE AREA.  $\uparrow$  MEANS THE HIGHER THE BETTER, WHILE  $\downarrow$  MEANS THE LOWER THE BETTER.

Method	fovea-central area					whole area				
	PSNR $\uparrow$	SSIM $\uparrow$	NMI $\uparrow$	FSIM $\uparrow$	LF $\downarrow$	PSNR $\uparrow$	SSIM $\uparrow$	NMI $\uparrow$	FSIM $\uparrow$	LF $\downarrow$
$w \setminus o$ <i>lf</i>	17.230 $\pm$ 0.081	<b>0.515</b> $\pm$ <b>0.007</b>	1.057 $\pm$ 0.001	0.675 $\pm$ 0.007	18.240 $\pm$ 0.068	17.403 $\pm$ 0.096	<b>0.556</b> $\pm$ <b>0.002</b>	1.062 $\pm$ 0.001	0.688 $\pm$ 0.003	18.258 $\pm$ 0.095
$w \setminus o$ <i>hf</i>	16.924 $\pm$ 0.076	0.393 $\pm$ 0.014	1.053 $\pm$ 0.001	0.584 $\pm$ 0.027	18.221 $\pm$ 0.024	17.461 $\pm$ 0.082	0.473 $\pm$ 0.018	1.062 $\pm$ 0.001	0.631 $\pm$ 0.013	18.156 $\pm$ 0.005
<b>FAUSRA (Ours)</b>	<b>17.487</b> $\pm$ <b>0.034</b>	<u>0.512</u> $\pm$ <u>0.007</u>	<b>1.057</b> $\pm$ <b>0.001</b>	<b>0.679</b> $\pm$ <b>0.004</b>	<b>18.150</b> $\pm$ <b>0.0144</b>	<b>17.679</b> $\pm$ <b>0.072</b>	<u>0.555</u> $\pm$ <u>0.002</u>	<b>1.063</b> $\pm$ <b>0.000</b>	<b>0.689</b> $\pm$ <b>0.003</b>	<b>18.124</b> $\pm$ <b>0.007</b>

TABLE III

RESULTS OF THE ABLATION STUDY ON THE CUHK-STDR OF FOVEA-CENTRAL AND WHOLE AREA.  $\uparrow$  MEANS THE HIGHER THE BETTER.

Method	fovea-central area				whole area			
	PSNR $\uparrow$	SSIM $\uparrow$	NMI $\uparrow$	FSIM $\uparrow$	PSNR $\uparrow$	SSIM $\uparrow$	NMI $\uparrow$	FSIM $\uparrow$
$w \setminus o$ <b>FAL</b>	17.172 $\pm$ 0.045	0.409 $\pm$ 0.016	1.055 $\pm$ 0.001	0.603 $\pm$ 0.013	17.610 $\pm$ 0.076	0.480 $\pm$ 0.006	1.063 $\pm$ 0.000	0.638 $\pm$ 0.003
$w \setminus o$ <b>FFCL</b>	17.335 $\pm$ 0.044	<b>0.516</b> $\pm$ <b>0.003</b>	1.055 $\pm$ 0.000	0.671 $\pm$ 0.001	17.393 $\pm$ 0.019	0.552 $\pm$ 0.002	1.060 $\pm$ 0.000	0.685 $\pm$ 0.002
$w \setminus$ <b>FFL</b> ( $w \setminus o$ <b>FFCL</b> )	17.442 $\pm$ 0.030	0.515 $\pm$ 0.001	1.056 $\pm$ 0.000	<b>0.680</b> $\pm$ <b>0.002</b>	17.573 $\pm$ 0.090	<b>0.557</b> $\pm$ <b>0.003</b>	1.062 $\pm$ 0.001	0.689 $\pm$ 0.001
<b>FAUSRA (Ours)</b>	<b>17.487</b> $\pm$ <b>0.034</b>	0.512 $\pm$ 0.007	<b>1.057</b> $\pm$ <b>0.001</b>	0.679 $\pm$ 0.004	<b>17.679</b> $\pm$ <b>0.072</b>	0.555 $\pm$ 0.002	<b>1.063</b> $\pm$ <b>0.000</b>	<b>0.689</b> $\pm$ <b>0.003</b>

In summary, we propose a GAN-based unpaired OCTA super-resolution. By leveraging spatial and frequency information, we improve the resolution while preserving *hf*. Our dual-path generators separately refine *hf* while retaining *hf* components, and the discriminators incorporate spatial and wavelets information as the **FAL**. We also introduce the **FFCL** to dynamically preserve the entire spectral consistency.

#### IV. EXPERIMENTAL EVALUATION

##### A. Dataset

The OCTA images used in this work were retrospectively collected from the Chinese University of Hong Kong Sight-Threatening Diabetic Retinopathy (CUHK-STDR) study. This study was an observational clinical study focused on diabetic retinal disease in subjects with Type 1 or Type 2 Diabetes Mellitus recruited from the CUHK Eye Centre and Hong Kong Eye Hospital [4], [7], [11], [48]. The OCTA imaging was performed using a swept-source optical coherence tomography (DRI OCT Triton; Topcon, Tokyo, Japan). Notably, CUHK-STDR dataset was paired, which could enable the training of unpaired models and evaluation using paired metrics.

Specifically, 296 pairs of fovea-central *HR* and *LR* OCTA images (see Fig. 1) were collected and split in the proportion of 4:1 for training and validation. Otherwise, additional 279 groups of paired *HR* and *LR* images for the whole area were also purposely collected and used for testing. Specifically, each group consisted of one *LR* and five *HR*. *HR* images included one fovea-center and four parafovea, which were combined to generate a whole *HR* 6mm $\times$ 6mm montage registered to the original *LR*. It is also worth noting that most typical OCTA images are fovea-centered in the real world; thus, we only utilized these data for testing. In the preprocessing of the training set, the original *LR* images were upsampled using bicubic interpolation (Fig. 1. A). We then cropped 256 $\times$ 256 patches from the upsampled *LR* images (Fig. 1. B) and corresponding *HR* images (Fig. 1. C). During the training phase, these cropped *LR* and *HR* patches were randomly selected and provided to the network in an unpaired manner. To prepare a pixel-wise aligned testing dataset for quantitative evaluation, each *LR* image was paired with an *HR* image from the same eye of the same patient. To account for slight structural changes due to the time interval between capturing

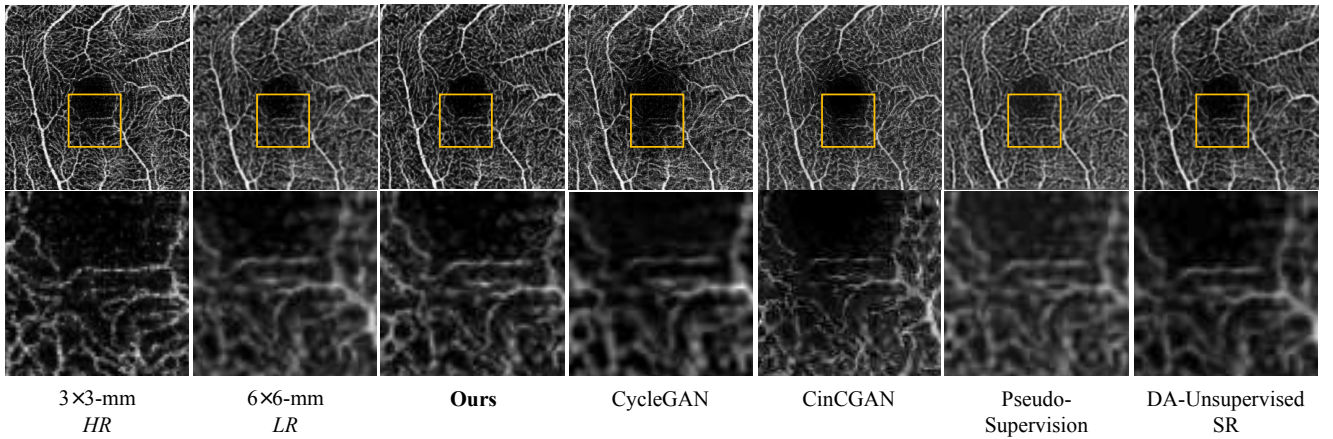


Fig. 6. Visual results of whole  $6\text{mm} \times 6\text{mm}$  OCTA image. The first and third rows are two exemplary reconstructed results. The second and fourth rows are zoomed in to local details.

the images, registration was performed to align the paired images. Thus, to evaluate the performance, the paired images were provided to the model after proper image registration.

### B. Implementation Details

Our model was trained on one NVIDIA RTX 3090 with 24GB memory. The parameters were initialized using the standard normal distribution. The initial learning rate was set to 0.0002, and it decayed linearly to 0 during training. The training phase optimized the parameters for a minimum of 5,000 iterations. In each iteration, an unaligned pair of  $HR$  and  $LR$  images was provided for the network. Specifically, the  $HR$  image was a  $3\text{mm} \times 3\text{mm}$  patch cropped with  $256 \text{ pixels} \times 256 \text{ pixels}$ , while the  $LR$  image was a  $6\text{mm} \times 6\text{mm}$  patch upsampled using bicubic interpolation and then randomly cropped with  $256 \text{ pixels} \times 256 \text{ pixels}$ .

We evaluated the performance using common pixel-wise paired metrics in super-resolution studies. Specifically, we used peak signal-to-noise ratio (PSNR), structural similarity index measure (SSIM) [49], normalized mutual information (NMI), and feature similarity index measure (FSIM) [50]. PSNR measured valid signals compared to noises. SSIM evaluated quality in terms of structure, illuminance, and contrast. NMI evaluated how matched the two images were. FSIM was a feature-level frequency-aware measurement that considered phase congruency and gradient magnitude.

### C. Experimental Results and Comparison

In Table. III-C, we compare our method to several baselines, including CycleGAN [24], Cycle-in-Cycle GAN (CinCGAN) [22], Pseudo-Supervision [23], and Domain Adaptation Unsupervised Super-Resolution (DA-Unsupervised SR) [28]. We also reimplement our previous work [47]. Similar to our approach, these baseline methods are all in the unpaired setting. The quantitative results demonstrate that our method outperforms them in most of the metrics and also surpasses our previous work.

Fig. 6 presents the visual results of our method. It shows how our approach improves the resolution of OCTA

images while preserving fine capillary structures. In comparison, CinCGAN introduces noise and loses the original vessel features. Pseudo-Supervision and DA-Unsupervised SR exhibit lower contrast compared to our method. CycleGAN successfully recovers  $hf$  vasculature but it disrupts the vessel coherence of the foveal avascular zone (FAZ). On the other hand, our method refines  $hf$  information while introducing minimal unexpected noise and retaining most of the original information. Notably, CinCGAN visually resembles the  $HR$  ground truth images (Fig. 7) with high SSIM and FSIM. However, the cost is the signal-to-noise ratio, as shown in Table. III-C. Therefore, our proposed approach achieves a better balance between structural information and the signal-to-noise ratio, resulting in overall higher fidelity.

### D. Frequency Decomposition in Generators

As previously illustrated in Fig. 4, we decompose  $hf$  and  $lf$  in generators to exceptionally enhance fine-grained details and alleviate  $lf$ -bias. Specifically,  $hf$  is provided for neural networks via  $HFB$  operation. Thus we further investigate the effectiveness of frequency decomposition.

First, as shown in Table. III-C, we respectively remove  $hf$  and  $lf$  by replacing frequency components with tensors filled with all zeros and freezing the gradients. Results show that either removing  $hf$  or  $lf$  would degrade the performance with respect to all metrics. Comparably, removing  $hf$  would lead to more severe degradation, especially in terms of FSIM. This confirms the  $lf$ -bias of the neural networks and verifies the effectiveness of our method.

Aside from evaluation in the spatial domain, we also examine the frequency domain by employing the Log Frequency Distance (LFD) metric [42], which is formed as:

$$LFD = \log \left[ \frac{1}{MN} \left( \sum_{m=0}^{M-1} \sum_{n=0}^{N-1} |F_x - F_y|^2 \right) + 1 \right] \quad (15)$$

where  $F_x$  and  $F_y$  are spectrums of generated and real images via Eq. (1).  $m$  and  $n$  are the Cartesian coordinates of the  $F$ . Eq. (15) measures the log mean square error over the whole spectrums. Table. III-C show different results as presented in Table. III-C. Reconstruction from components *w/o*  $lf$  leads

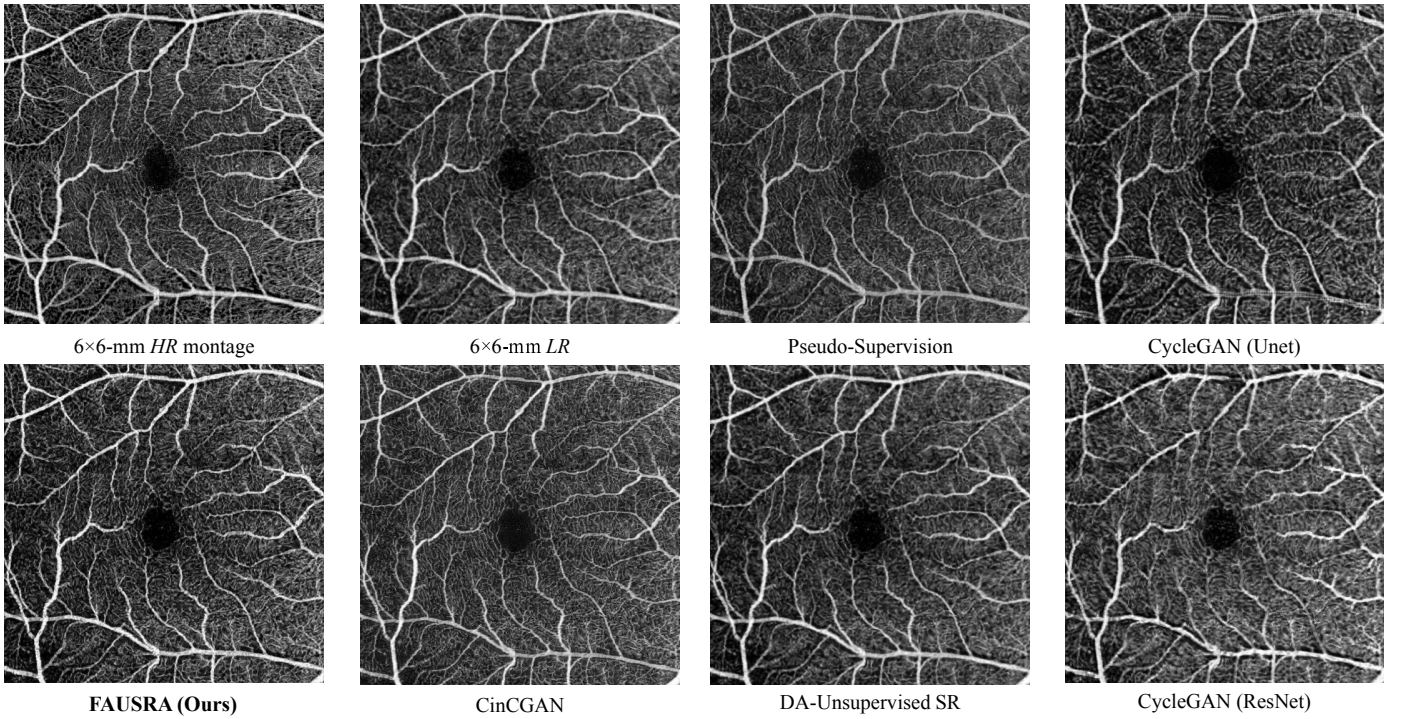


Fig. 7. Visual results of whole 6mm  $\times$  6mm OCTA image. The first and third rows are two exemplary reconstructed results. The second and fourth rows are zoomed in to local details.

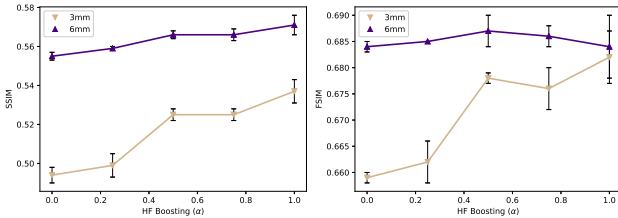


Fig. 8. Plots of the *HFB* rates versus different qualitative metrics.

to higher spectral errors than results from *w/o hf*. This may be attributed to the common view that most spectral powers are concentrated in *lf* bands [51]. Thus although the spectral errors for *hf* are less than that for *lf*, these comparably slight disturbances for *hf* would lead to more severe quality degradation in spatial domain images. Results verify the necessity to exceptionally emphasize *hf* while preserving *lf*.

Moreover, we also evaluate the effectiveness of *HFB* in Eq. (4). As shown in Fig. 8, results illustrate the relationship between qualitative performance and the level of boosting, which is  $\alpha$  in Eq. (4). We observe better performances in terms of SSIM and FSIM as more *hf* information is provided. This indicates that *hf* components play a crucial role in preserving structural information. The above results demonstrate the significance of our *HFB* operation in frequency decomposition.

### E. Frequency-Aware Loss Functions

We introduce two frequency-aware loss functions, which are Frequency-aware Focal Consistency Loss (FFCL) and

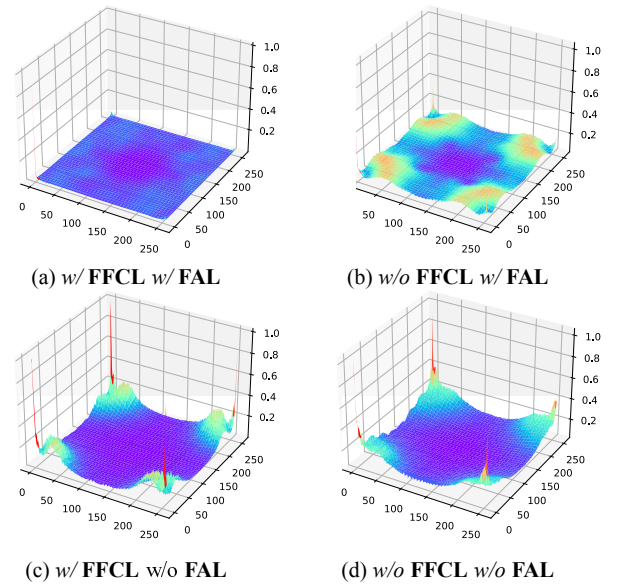


Fig. 9. 3D visualization for spectral errors. The horizontal plane is the spectrum coordinates, while the vertical axis indicates the error intensity. Larger errors indicate less accurately reconstructed frequencies.

Frequency-Aware Adversarial Loss (FAL). They were designed to provide more precise supervision over the spectrum. To verify the effectiveness, we present the 3D visualization for errors in the spectrum for different results obtained using FFCL and FAL, as shown in Fig. 9. It can be observed that without FFCL and FAL, most of the spectral errors are introduced by the *hf* components. This indicates the importance



of addressing the frequency information for accurate spectral reconstruction. By incorporating **FAL**, the discriminators help the model become more aware of the *hf* components and reduce the corresponding reconstruction errors. However, there are still inaccuracies in the middle- to high-frequency components. Otherwise, **FFCL** retains more precise middle-frequency information but lacks the capability to reproduce *hf* accurately. Consequently, by leveraging both **FFCL** and **FAL**, our super-resolution model is able to maintain precise results across the entire spectrum. This combined approach effectively addresses the challenges posed by different frequency components and enhances spectral precision.

#### F. Ablation Study

To evaluate the effects of different components, we continue to conduct ablation on **FAL** and **FFCL**, as shown in Table III-C. By removing the **FAL** and the **FFCL**, we observed a decline or similar performance in PSNR, particularly in the fovea-central area. This indicates that the frequency-aware losses applied to the generators and discriminators play a crucial role in controlling the noise intensity. These findings are consistent with the results in Fig. 6. Furthermore, we replaced the proposed **FFCL** with focal frequency loss (**FFL**) [42]. Comparing the results, we found that **FFL** can preserve the structural information related to *hf* components, but our proposed **FFCL** achieves higher accuracy in preserving the structural details. These results empirically evidence the effectiveness of each component in our approach, showcasing contributions to reconstructing high-quality images in both the spatial and frequency domains.

#### V. DISCUSSION

This paper proposed a GAN-based approach for unpaired OCTA image super-resolution. We formulated restoration and degradation GANs and optimized the models end-to-end through consistency regularization. Meanwhile, since fine-grained features such as capillaries in microvasculature are critical biomarkers for ophthalmology studies, we leveraged frequency and spatial information to mitigate the *lf*-bias of neural networks and enhance *hf*. We verified the general performance and effectiveness of our approach through quantitative results and visualization from various experiments.

However, since the unpaired super-resolution setting lacks pixel-wise supervision information, the overall performance might not be comparable to fully supervised approaches [9], [16], [17]. As shown in Fig. 6, although our method could enhance the intensities of *hf* capillary details without introducing extra artifacts, it could not precisely infer missing semantic information and might lead to vessel incoherence.

Another limitation of current approaches, including our proposed method, was the assumption that the features inside and outside the fovea-central 3mm×3mm area are identically distributed because only this region could provide *HR* supervision information. However, this assumption is not solid and may impede the generalizability of the model. One possible solution is to formulate a self-supervised learning approach, such as image inpainting, to infer and fill in missing information in peripheral regions [52].

#### VI. CONCLUSION

This paper presented a novel approach, Frequency-aware Unpaired Super-Resolution for OCTA images (FAUSRA), for enhancing the resolution using the unpaired setting. We proposed a GAN-based framework to mimic restoration and degradation mappings, optimized end-to-end through consistency loss. Given the importance of fine-grained capillaries in microvasculature as biomarkers for OCTA, we employed frequency decomposition to emphasize *hf* by separating and fusing frequency components. We also introduced an **FAL** for the discriminators to better preserve the capillary structure, and an **FFCL** to preserve the spectrum consistency. We conducted experiments and analytical studies to validate the effectiveness of the method and to show the superior performance. To the best of our knowledge, as an extension of our previous work [47], our studies were the first to leverage frequency analysis and to utilize GAN in unpaired OCTA super-resolution. It addressed challenges associated with large-scale data collection and complex data preparation required in conventional supervised super-resolution methods in the perspective of frequency-domain analysis.

#### REFERENCES

- [1] Y. Jia, S. T. Bailey, T. S. Hwang, S. M. McClintic, S. S. Gao, M. E. Pennesi, C. J. Flaxel, A. K. Lauer, D. J. Wilson, J. Hornegger *et al.*, "Quantitative optical coherence tomography angiography of vascular abnormalities in the living human eye," *Proceedings of the National Academy of Sciences*, vol. 112, no. 18, pp. E2395–E2402, 2015.
- [2] T. S. Hwang, Y. Jia, S. S. Gao, S. T. Bailey, A. K. Lauer, C. J. Flaxel, D. J. Wilson, and D. Huang, "Optical coherence tomography angiography features of diabetic retinopathy," *Retina (Philadelphia, Pa.)*, vol. 35, no. 11, p. 2371, 2015.
- [3] L. Roisman, Q. Zhang, R. K. Wang, G. Gregori, A. Zhang, C.-L. Chen, M. K. Durbin, L. An, P. F. Stetson, G. Robbins *et al.*, "Optical coherence tomography angiography of asymptomatic neovascularization in intermediate age-related macular degeneration," *Ophthalmology*, vol. 123, no. 6, pp. 1309–1319, 2016.
- [4] Z. Sun, F. Tang, R. Wong, J. Lok, S. K. Szeto, J. C. Chan, C. K. Chan, C. C. Tham, D. S. Ng, and C. Y. Cheung, "Oct angiography metrics predict progression of diabetic retinopathy and development of diabetic macular edema: a prospective study," *Ophthalmology*, vol. 126, no. 12, pp. 1675–1684, 2019.
- [5] H. Che, H. Jin, and H. Chen, "Learning robust representation for joint grading of ophthalmic diseases via adaptive curriculum and feature disentanglement," in *International Conference on Medical Image Computing and Computer-Assisted Intervention*. Springer, 2022, pp. 523–533.
- [6] H. Che, Y. Cheng, H. Jin, and H. Chen, "Towards generalizable diabetic retinopathy grading in unseen domains," *arXiv preprint arXiv:2307.04378*, 2023.
- [7] D. Yang, Z. Tang, A. Ran, T. X. Nguyen, S. Szeto, J. Chan, C. Y. Wong, V. Hui, K. Tsang, C. K. Chan *et al.*, "Assessment of parafoveal diabetic macular ischemia on optical coherence tomography angiography images to predict diabetic retinal disease progression and visual acuity deterioration," *JAMA ophthalmology*, 2023.
- [8] R. F. Spaide, J. G. Fujimoto, N. K. Waheed, S. R. Sadda, and G. Staurenghi, "Optical coherence tomography angiography," *Progress in retinal and eye research*, vol. 64, pp. 1–55, 2018.
- [9] M. Gao, Y. Guo, T. Hormel, J. Sun, T. Hwang, and Y. Jia, "Reconstruction of high-resolution 6×6-mm oct angiograms using deep learning," *Biomedical Optics Express*, vol. 11, pp. 3585–3600, 06 2020.
- [10] S. S. Gao, Y. Jia, M. Zhang, J. P. Su, G. Liu, T. S. Hwang, S. T. Bailey, and D. Huang, "Optical coherence tomography angiography," *Investigative ophthalmology & visual science*, vol. 57, no. 9, pp. OCT27–OCT36, 2016.
- [11] D. Yang, Z. Tang, F. Tang, S. Szeto, J. Chan, F. Yip, C. Wong, A. Ran, T. Lai, and C. Cheung, "Clinically relevant factors associated with a binary outcome of diabetic macular ischaemia: an octa study." *The British Journal of Ophthalmology*, 2022.

- [12] Z. Nafar, T. Callan, W. Lewis, and T. Bacci, "Clinical benefits of a new swept-source oct angio hd6x6 mm scan compared to angio 3x3 mm scan," *Investigative Ophthalmology & Visual Science*, vol. 62, no. 8, pp. 1875–1875, 2021.
- [13] J. Ho, K. Dans, Q. You, E. D. Nudleman, and W. R. Freeman, "Comparison of 3 mm × 3 mm versus 6 mm × 6 mm optical coherence tomography angiography scan sizes in the evaluation of non-proliferative diabetic retinopathy," *Retina*, vol. 39, pp. 259–264, 02 2019.
- [14] T. Ziqi, X. Wang, A. Ran, F. Tang, Y. Cai, H. Che, D. G. YANG, L. Luo, Q. Liu, Y. L. Wong *et al.*, "Using deep learning for assessing image-quality of 3d macular scans from spectral-domain optical coherence tomography," *Investigative Ophthalmology & Visual Science*, vol. 63, no. 7, pp. 204–F0051, 2022.
- [15] H. Che, S. Chen, and H. Chen, "Image quality-aware diagnosis via meta-knowledge co-embedding," in *Proceedings of the IEEE/CVF Conference on Computer Vision and Pattern Recognition*, 2023, pp. 19 819–19 829.
- [16] M. Gao, T. Hormel, J. Wang, Y. Guo, S. Bailey, T. Hwang, and Y. Jia, "An open-source deep learning network for reconstruction of high-resolution oct angiograms of retinal intermediate and deep capillary plexuses," *Investigative Ophthalmology & Visual Science*, vol. 62, pp. 1032–1032, 11 2021.
- [17] H. Hao, C. Xu, D. Zhang, Q. Yan, J. Zhang, Y. Liu, and Y. Zhao, "Sparse-based domain adaptation network for octa image super-resolution reconstruction," *IEEE Journal of Biomedical and Health Informatics*, vol. 26, no. 9, pp. 4402–4413, 2022.
- [18] P. Paavilainen, S. U. Akram, and J. Kannala, "Bridging the gap between paired and unpaired medical image translation," in *MICCAI Workshop on Deep Generative Models*. Springer, 2021, pp. 35–44.
- [19] A. Bulat, J. Yang, and G. Tzimiropoulos, "To learn image super-resolution, use a gan to learn how to do image degradation first," in *Proceedings of the European conference on computer vision (ECCV)*, 2018, pp. 185–200.
- [20] I. Goodfellow, J. Pouget-Abadie, M. Mirza, B. Xu, D. Warde-Farley, S. Ozair, A. Courville, and Y. Bengio, "Generative adversarial networks," *Communications of the ACM*, vol. 63, no. 11, pp. 139–144, 2020.
- [21] T. Zhao, W. Ren, C. Zhang, D. Ren, and Q. Hu, "Unsupervised degradation learning for single image super-resolution," *arXiv preprint arXiv:1812.04240*, 2018.
- [22] Y. Yuan, S. Liu, J. Zhang, Y. Zhang, C. Dong, and L. Lin, "Unsupervised image super-resolution using cycle-in-cycle generative adversarial networks," in *Proceedings of the IEEE Conference on Computer Vision and Pattern Recognition Workshops*, 2018, pp. 701–710.
- [23] S. Maeda, "Unpaired image super-resolution using pseudo-supervision," in *Proceedings of the IEEE/CVF Conference on Computer Vision and Pattern Recognition*, 2020, pp. 291–300.
- [24] J.-Y. Zhu, T. Park, P. Isola, and A. A. Efros, "Unpaired image-to-image translation using cycle-consistent adversarial networks," in *Proceedings of the IEEE international conference on computer vision*, 2017, pp. 2223–2232.
- [25] Y. Xie, D. Yang, A. S. Huang, Y. Yang, Y. Han, Y. Sun, K. Cao, H. Wang, S. Wu, Q. Zhu *et al.*, "Retinal microvasculature is a potential biomarker for acute mountain sickness," *Science China Life Sciences*, pp. 1–13, 2023.
- [26] Y. Ma, H. Hao, J. Xie, H. Fu, J. Zhang, J. Yang, Z. Wang, J. Liu, Y. Zheng, and Y. Zhao, "Rose: A retinal oct-angiography vessel segmentation dataset and new model," *IEEE Transactions on Medical Imaging*, vol. 40, no. 3, pp. 928–939, 2021.
- [27] Z.-Q. J. Xu, Y. Zhang, T. Luo, Y. Xiao, and Z. Ma, "Frequency principle: Fourier analysis sheds light on deep neural networks," *arXiv preprint arXiv:1901.06523*, 2019.
- [28] W. Wang, H. Zhang, Z. Yuan, and C. Wang, "Unsupervised real-world super-resolution: A domain adaptation perspective," in *Proceedings of the IEEE/CVF International Conference on Computer Vision*, 2021, pp. 4318–4327.
- [29] X. Ji, G. Tao, Y. Cao, Y. Tai, T. Lu, C. Wang, J. Li, and F. Huang, "Frequency consistent adaptation for real world super resolution," in *Proceedings of the AAAI Conference on Artificial Intelligence*, vol. 35, no. 2, 2021, pp. 1664–1672.
- [30] Y. Tai, J. Yang, and X. Liu, "Image super-resolution via deep recursive residual network," in *Proceedings of the IEEE conference on computer vision and pattern recognition*, 2017, pp. 3147–3155.
- [31] C. Dong, C. C. Loy, K. He, and X. Tang, "Learning a deep convolutional network for image super-resolution," in *European conference on computer vision*. Springer, 2014, pp. 184–199.
- [32] Y. Wei, S. Gu, Y. Li, R. Timofte, L. Jin, and H. Song, "Unsupervised real-world image super resolution via domain-distance aware training," in *Proceedings of the IEEE/CVF Conference on Computer Vision and Pattern Recognition*, 2021, pp. 13 385–13 394.
- [33] C. Ledig, L. Theis, F. Huszar, J. Caballero, A. Cunningham, A. Acosta, A. Aitken, A. Tejani, J. Totz, Z. Wang *et al.*, "Photo-realistic single image super-resolution using a generative adversarial network," in *Proceedings of the IEEE conference on computer vision and pattern recognition*, 2017, pp. 4681–4690.
- [34] X. Ji, Y. Cao, Y. Tai, C. Wang, J. Li, and F. Huang, "Real-world super-resolution via kernel estimation and noise injection," in *proceedings of the IEEE/CVF conference on computer vision and pattern recognition workshops*, 2020, pp. 466–467.
- [35] S. Chen, Z. Han, E. Dai, X. Jia, Z. Liu, L. Xing, X. Zou, C. Xu, J. Liu, and Q. Tian, "Unsupervised image super-resolution with an indirect supervised path," in *Proceedings of the IEEE/CVF Conference on Computer Vision and Pattern Recognition Workshops*, 2020, pp. 468–469.
- [36] Z. Wang, J. Chen, and S. C. Hoi, "Deep learning for image super-resolution: A survey," *IEEE transactions on pattern analysis and machine intelligence*, vol. 43, no. 10, pp. 3365–3387, 2020.
- [37] S. Yamaguchi and S. Kanai, "F-drop&match: Gans with a dead zone in the high-frequency domain," in *Proceedings of the IEEE/CVF International Conference on Computer Vision*, 2021, pp. 6743–6751.
- [38] M. Khayatkhoei and A. Elgammal, "Spatial frequency bias in convolutional generative adversarial networks," in *Proceedings of the AAAI Conference on Artificial Intelligence*, vol. 36, no. 7, 2022, pp. 7152–7159.
- [39] M. Cai, H. Zhang, H. Huang, Q. Geng, Y. Li, and G. Huang, "Frequency domain image translation: More photo-realistic, better identity-preserving," in *Proceedings of the IEEE/CVF International Conference on Computer Vision*, 2021, pp. 13 930–13 940.
- [40] K. Xu, M. Qin, F. Sun, Y. Wang, Y.-K. Chen, and F. Ren, "Learning in the frequency domain," in *Proceedings of the IEEE/CVF Conference on Computer Vision and Pattern Recognition (CVPR)*, June 2020.
- [41] M. Fritsche, S. Gu, and R. Timofte, "Frequency separation for real-world super-resolution," in *2019 IEEE/CVF International Conference on Computer Vision Workshop (ICCVW)*. IEEE, 2019, pp. 3599–3608.
- [42] L. Jiang, B. Dai, W. Wu, and C. C. Loy, "Focal frequency loss for image reconstruction and synthesis," in *Proceedings of the IEEE/CVF International Conference on Computer Vision*, 2021, pp. 13 919–13 929.
- [43] R. Durall, M. Keuper, and J. Keuper, "Watch your up-convolution: Cnn based generative deep neural networks are failing to reproduce spectral distributions," in *Proceedings of the IEEE/CVF conference on computer vision and pattern recognition*, 2020, pp. 7890–7899.
- [44] V. Singh, A. Sharma, S. Devanathan, and A. Mittal, "High-frequency refinement for sharper video super-resolution," in *Proceedings of the IEEE/CVF Winter Conference on Applications of Computer Vision*, 2020, pp. 3299–3308.
- [45] X. Mao, Q. Li, H. Xie, R. Y. Lau, Z. Wang, and S. Paul Smolley, "Least squares generative adversarial networks," in *Proceedings of the IEEE international conference on computer vision*, 2017, pp. 2794–2802.
- [46] K. He, X. Zhang, S. Ren, and J. Sun, "Deep residual learning for image recognition," in *Proceedings of the IEEE conference on computer vision and pattern recognition*, 2016, pp. 770–778.
- [47] W. Zhang, D. Yang, C. Y. Cheung, and H. Chen, "Frequency-aware inverse-consistent deep learning for oct-angiogram super-resolution," in *Medical Image Computing and Computer Assisted Intervention—MICCAI 2022: 25th International Conference, Singapore, September 18–22, 2022, Proceedings, Part II*. Springer, 2022, pp. 645–655.
- [48] F. Y. Tang, D. S. Ng, A. Lam, F. Luk, R. Wong, C. Chan, S. Mohamed, A. Fong, J. Lok, T. Tso *et al.*, "Determinants of quantitative optical coherence tomography angiography metrics in patients with diabetes," *Scientific reports*, vol. 7, no. 1, pp. 1–10, 2017.
- [49] Z. Wang, A. C. Bovik, H. R. Sheikh, and E. P. Simoncelli, "Image quality assessment: from error visibility to structural similarity," *IEEE transactions on image processing*, vol. 13, no. 4, pp. 600–612, 2004.
- [50] L. Zhang, L. Zhang, X. Mou, and D. Zhang, "Fsim: A feature similarity index for image quality assessment," *IEEE transactions on Image Processing*, vol. 20, no. 8, pp. 2378–2386, 2011.
- [51] K. Chandrasegaran, N.-T. Tran, and N.-M. Cheung, "A closer look at fourier spectrum discrepancies for cnn-generated images detection," in *Proceedings of the IEEE/CVF conference on computer vision and pattern recognition*, 2021, pp. 7200–7209.
- [52] D. Pathak, P. Krahenbuhl, J. Donahue, T. Darrell, and A. A. Efros, "Context encoders: Feature learning by inpainting," in *Proceedings of the IEEE conference on computer vision and pattern recognition*, 2016, pp. 2536–2544.